

Comparing Convective Self-Aggregation in Idealized Models to Observed Moist Static Energy Variability near the Equator

Tom Beucler ^{1,2}, Tristan H. Abbott ³, Timothy W. Cronin ³, Michael S. Pritchard ¹

¹Department of Earth System Science, University of California, Irvine, CA, USA

²Department of Earth and Environmental Engineering, Columbia University, New York, NY, USA

³Department of Earth, Atmospheric and Planetary Sciences, MIT, Cambridge, MA, USA

Key Points:

- Moist static energy zonal spectral tendencies have similar signs and scale-selectivity in convection-permitting models and observations.
- Radiation increases variance at long wavelengths while surface enthalpy fluxes and advection reduce variance.

arXiv:1908.03764v1 [physics.ao-ph] 10 Aug 2019

Abstract

Idealized convection-permitting simulations of radiative-convective equilibrium (RCE) have become a popular tool for understanding the physical processes leading to horizontal variability of tropical water vapor and rainfall. However, the applicability of idealized simulations to nature is still unclear given that important processes are typically neglected, such as lateral vapor advection by extratropical intrusions, or interactive ocean coupling. Here, we exploit spectral analysis to compactly summarize the multi-scale processes supporting convective aggregation. By applying this framework to high-resolution reanalysis data and satellite observations in addition to idealized simulations, we compare convective-aggregation processes across horizontal scales and datasets. The results affirm the validity of the RCE simulations as an analogy to the real world. Column moist static energy tendencies share similar signs and scale-selectivity in convection-permitting models and observations: Radiation increases variance at wavelengths above 1,000km, while advection damps variance across wavelengths, and surface fluxes mostly reduce variance between 1,000km and 10,000km.

Plain Language Summary

Advances in computing have allowed computer models to simulate tropical weather systems spanning a few dozen kilometers at the same time as moist and dry regions spanning several thousand kilometers. To improve and validate computer models, we need to compare computer simulations to real-world observations, but we lack a compact way of simultaneously comparing them at scales close to 10km, 100km, 1,000km, and 10,000km. By breaking down water vapor variability near the Equator into contributions from these different length scales, we can identify the scales at which computer models agree with real-world observations and explain why. Surprisingly, even computer models that are run in a highly idealized configuration compare well against observations of the real world, despite the fact that nature never attains this idealized limit. We find that atmospheric radiation tends to intensify moist and dry regions of several thousand kilometers near the Equator, while lateral transport of energy and surface-atmosphere exchanges tend to smooth out these moist and dry regions.

1 Introduction

Tropical weather and climate are strongly shaped by the variability of column water vapor, which dominates column-integrated moist static energy (MSE) variability due to weak horizontal variations in tropical atmospheric temperature. On meteorological timescales, the intensity of extreme precipitation events depends on the humidity and temperature of the surrounding environment, e.g. for isolated convective cells, mesoscale convective systems (LeMone et al., 1998) and tropical cyclones (Hill & Lackmann, 2009). On climatic timescales, the zonal variability of MSE is linked to the equator-to-pole energy transport (Trenberth et al., 2002) and to climate sensitivity through the link between the hydrological cycle and cloud and water vapor feedbacks (Feldl et al., 2014). Persistent regions of high and low MSE occur due to surface heterogeneities, including ocean currents, continents, and mountain ranges (Figure 1a), while transient anomalies in MSE near the Equator (e.g., Figure 1c) relate to a rich spectrum of tropical weather across a range of temporal and spatial scales. This includes isolated convective activity (~ 1 hour, ~ 10 km), mesoscale convective complexes (~ 10 hours, ~ 100 km) (e.g. review by Houze, 2004), tropical depressions (~ 10 days, ~ 1000 km) (e.g. review by Montgomery & Smith, 2017), the Madden-Julian Oscillation (e.g. review by Zhang, 2005), and the Asian monsoon (~ 60 days, ~ 10000 km) (e.g. review by Webster et al., 1998).

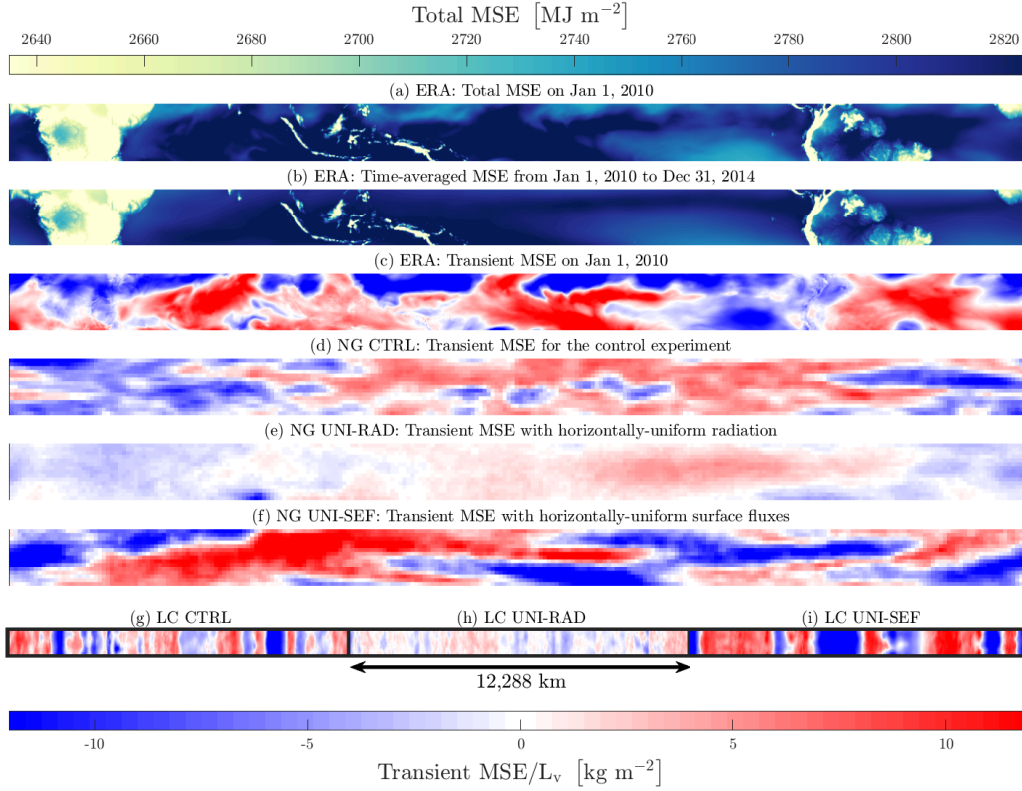


Figure 1. (a) Instantaneous, (b) time-averaged, and (c) transient MSE in ERA from 10°S to 10°N. (d-i) Instantaneous transient MSE in each model of section 2. Transient MSE is normalized by the latent heat of vaporization of water L_v to yield units kg m^{-2} : the length of the bottom colorbar corresponds to $\sim 60\text{MJ m}^{-2}$. Panels (a-f) respect the original aspect ratio of the horizontal domain. While the length of the long-channel equals a third of the Equator’s length, its width has been multiplied by a factor 5 in panels (g-i) to facilitate visualization.

Advanced computing now allows simulation of planetary-scale domains ($\sim 10^4$ km) with convection-permitting models (CPM) of horizontal resolution ~ 1 km, which can resolve this entire spectrum of tropical weather. Tropical weather systems have been extensively compared in field-campaign observations and regional CPM to evaluate CPMs’ ability to adequately represent convective processes (e.g., Beucher et al., 2014; Laing et al., 2012; Woodhams et al., 2018). However, explicit comparisons of physical processes regulating the spatio-temporal spectrum of MSE in observations and CPM are rare. The goal of this paper is to use a spectral budget for sources and sinks of transient MSE variance as a step towards comparing these physical processes across observations and models of varying complexity.

We use the column-integrated frozen moist static energy H (units J m^{-2}):

$$H(x, y, t) \stackrel{\text{def}}{=} \int_0^{p_s} \frac{dp}{g} \left(L_v q - L_f q_i + \underbrace{c_p T + gz}_s \right), \quad (1)$$

as a diagnostic because it is approximately conserved during convection, and because previous studies in idealized CPM have successfully used its variance budget to assess processes that favor or disfavor convective aggregation (e.g., Wing & Emanuel, 2014; Wing & Cronin, 2016). Here, p_s is surface pressure and p the mean pressure profile,

L_v and L_f are the latent heat of vaporization and fusion of water, respectively, q and q_i are water vapor and ice mixing ratios, respectively, c_p is the specific heat capacity of dry air at constant pressure, T is the absolute temperature, g is the gravity constant, z is the geopotential height, and s is the dry static energy. The total MSE field H has spatial variability in its temporal mean \overline{H} , as well as spatiotemporal variability in the transient MSE anomaly H' , here defined by:

$$H(x, y, t) = \overline{H}(x, y) + H'(x, y, t) \quad (2)$$

Note that transient MSE variability may be modulated nonlinearly by the stationary MSE features, adding another level of complexity to MSE transients — but in this paper we will focus primarily on comparing transient MSE variability across models and observations without directly assessing this role of nonlinear modulation.

Previous work (e.g., Held et al., 1993; Muller & Bony, 2015) has consistently found that when CPMs are run on large enough domains, MSE self-organizes into moist and dry regions even in the absence of external forcing (such as planetary rotation, surface inhomogeneities or large-scale wind shear). This emergent property of moist convection, referred to as “convective self-aggregation” (e.g., review by Wing et al., 2017; Holloway et al., 2017), suggests that a significant fraction of transient MSE variability near the Equator might arise from internal self-organization rather than external processes such as surface characteristics, teleconnections with the mid-latitudes, or ocean coupling. The problem is that physical mechanisms of convective self-aggregation have been extensively studied in the context of idealized CPM with fixed surface temperatures, which ignore external processes, and thus provide an uncertain analogy to real-world settings.

This motivates the aim of our paper — quantitatively comparing convective-aggregation processes in idealized CPM and observations. This comparison may deepen our understanding of (1) how transient MSE anomalies grow and decay and (2) how valid idealized CPM simulations are as an analogy to the real world. Idealized CPM have been compared to observations in the past, but mostly at coarse granularity by looking for similar correlations or distributions of variables. Using satellite data, Tobin et al. (2012) showed that ($10^\circ \times 10^\circ$) longitude-latitude boxes with more convective organization also exhibited lower values of MSE and larger outgoing longwave radiation, consistent with idealized CPM experiments (Wing & Emanuel, 2014). Holloway et al. (2017) used data from the Nauru meteorological station and showed that the long-channel configuration of Wing & Cronin (2016) had more realistic distributions of MSE and vertical velocity than traditional square-domain CPM. Additionally, Stein et al. (2017) showed that for a given large-scale precipitation rate and vertical motion, anvil clouds decreased with the degree of aggregation in satellite data, while low clouds and precipitation efficiency increased with aggregation, consistent with CPM simulations (e.g., Figure 8 of Wing & Cronin, 2016). Recently, Holloway (2017) used the MSE spatial variance budget to show that interactive radiation maintained aggregation while MSE advection disaggregated convection in CPM experiments forced using satellite data, as found in idealized CPM simulations of RCE.

While Holloway’s simulations support the validity of the RCE analogy, their small domain size ($10^\circ \times 10^\circ$) may underestimate convective-aggregation feedbacks because of the effect of MSE advection from the prescribed boundary conditions. Motivated by the recent availability of planetary-domain CPM and high-resolution reanalysis products, we proceed by comparing the observed transient MSE field (Figure 1c) to the transient MSE field from several idealized, large-domain CPM experiments (Wing et al., 2017; Khairoutdinov & Emanuel, 2018, Figures 1d-i) and ask:

How do the physical processes that regulate observed moist static energy variance compare to the convective-aggregation processes from idealized models *at each horizontal scale*?

The work below is organized as follows. After introducing the observational and model datasets in section 2, we investigate the zonal power spectra of transient MSE and how they evolve under the influence of radiation, surface enthalpy fluxes, and advection in section 3, before concluding in section 4.

2 Data

We use four datasets to compare convective aggregation in observations and idealized CPM: Meteorological reanalysis (ERA), satellite observations (CERES), a rotating near-global simulation (NG) and a non-rotating long-channel simulation (LC). A snapshot of the transient MSE field from each is shown in Figure 1, and each is described in more detail below.

2.1 Reanalysis observations: ERA

The European Centre for Medium-Range Weather Forecasts Re-Analysis (ERA) version 5 (Hersbach & H., 2016) was produced by assimilating observational data in version CY41R2 of the Integrated Forecast System. The new reanalysis dataset has a better hydrological cycle and sea surface temperatures in the Tropics and is calibrated for climate applications. Zonal and temporal resolutions are $27.5\text{km} \times 1\text{hour}$.

2.2 Satellite observations: CERES

The Clouds & Earth’s Radiant Energy Systems (CERES, Wielicki et al., 1996) “CERES SYN1deg Ed4A” dataset provides diurnally-complete top-of-atmosphere and surface radiative fluxes by using sixteen geostationary satellites as well as the National Aeronautics and Space Administration’s Moderate Resolution Imaging Spectroradiometer. Zonal and temporal resolutions are $1^\circ \times 1\text{hour}$.

2.3 Convection-permitting Model (CPM) Simulations

The following experiments were conducted using the System for Atmospheric Modeling (SAM), a convection-permitting model that is widely used for idealized studies, solves the anelastic equations of motion, and includes cloud microphysics and subgrid turbulence parameterizations (Khairoutdinov & Randall, 2003).

- **LC:** A suite of three idealized long-channel (LC) experiments with a doubly-periodic horizontal domain of size $12,288 \times 192\text{km}^2$ over a uniform ocean surface with temperature 300K, using SAM v6.8.2. These consist of a control simulation (LC CTRL, Figure 1g), described in Wing & Cronin (2016), and simulations that horizontally homogenize either radiation (LC UNI-RAD, Figure 1h), or surface enthalpy fluxes (LC UNI-SEF, Figure 1i), described in Beucler & Cronin (2018). Each experiment was run for 80 days to a statistically steady state and outputs were saved with zonal and temporal resolutions of $3\text{km} \times 1\text{hour}$.
- **NG:** Similar to LC, but for a much larger (near-global; NG, $40,360 \times 10,000\text{km}^2$) ocean-only, zonally-periodic domain with prescribed ocean surface temperatures that decrease away from the equator and a Coriolis parameter that increases away from the equator, allowing for formation of extratropical eddies which intrude into the tropics. As with LC, three runs were conducted at 300K, consisting of NG CTRL (control experiment, Figure 1d), NG UNI-RAD (horizontally-uniform radiative heating, Figure 1e) and NG UNI-SEF (horizontally-uniform surface enthalpy fluxes, Figure 1f) in Khairoutdinov & Emanuel (2018). Each experiment was run for a year, using SAM v6.10.6. Outputs were saved with zonal and temporal resolutions of $156.25\text{km} \times 1\text{day}$.

At spatial scales below O (100km), most of the spatial variance comes from sub-diurnal variability from isolated convective events (not shown). Hence, to make meaningful comparisons across datasets, we time-average the fields of ERA, CERES and LC over one-day blocks before calculating spatial co-spectra using the Fast Fourier Transform algorithm (Frigo & Johnson, 2005).

3 Zonal Spectral Budget of Transient Column Moist Static Energy

The following spectral method will allow us to (1) separate the zonal variability of MSE in each dataset into contributions from different scales and (2) quantify the amount of variance created by radiation, surface enthalpy fluxes, and advection at each zonal scale. Specifically, we measure zonal variability of transient MSE H' at a given zonal wavelength λ using the zonal power spectrum φ_H of transient MSE, defined as:

$$\varphi_H(\lambda, y, t) \stackrel{\text{def}}{=} \widehat{H'}^* \widehat{H'}, \quad (3)$$

where t is time and $\widehat{H'}$ is the zonal Fourier transform of the transient MSE field H' :

$$\widehat{H'}(\lambda, y, t) \stackrel{\text{def}}{=} \frac{1}{\sqrt{2\pi}} \int_0^{L(y)} \exp\left(-\frac{2\pi i x}{\lambda}\right) H'(x, y, t) dx, \quad (4)$$

where i is the unit imaginary number and $L(y)$ is the length of the latitude circles of ordinate y in all cases but LC, for which $L(y)$ is the periodic domain's length. From φ_H , one can calculate various aspects of the transient MSE zonal variability, including its spectral-mean wavelength (equation 2 of Beucler & Cronin (2018)) and its total (i.e. wavenumber-integrated) zonal variance.

3.1 Zonal Power Spectra

Figure 2a shows φ_H for two LC experiments:

1. The control experiment CTRL (full lines): This experiment is initialized with a horizontally uniform sounding taken from small-domain RCE, but moist and dry regions of finite size ($\sim 2,000\text{km}$) and MSE anomalies ($\sim 7\text{kg m}^{-2} \times L_v$) spontaneously form after $\sim 1\text{month}$ despite homogeneous boundary conditions¹. Although the temporal variations of the transient MSE field appear complicated in physical space, Figure 2a reveals a simpler picture in spectral space: As convection self-aggregates (i.e. progressing from solid purple to yellow lines²), MSE variance increases at wavelengths above $\lambda \sim 100\text{km}$ before equilibrating with a variance peak at $\lambda \sim 2,000\text{km}$, explaining why anomalies of this scale are most visible in Figure 1g. Note that the y-axis of Figure 2a is logarithmic so the total variance in the aggregated state (solid yellow line) is dominated by the $\lambda \sim 2,000\text{km}$ variance peak.
2. The UNI-RAD experiment (dotted lines): Horizontally homogenizing radiative heating greatly weakens aggregation, as evidenced by reduced MSE perturbations ($\sim 2\text{kg m}^{-2} \times L_v$). Unlike the CTRL experiment, MSE variance only grows at the longest wavelengths for the first 10 days before stabilizing around $1 - 2\text{kg}^2 \text{m}^{-4} \times L_v^2$. Using UNI-RAD as our reference “non-aggregated” experiment³, the effect of self-aggregation can then be quantified as the difference between the full and dotted yellow lines, and is only significant on scales larger than $\lambda \sim 1,000\text{km}$.

¹ See Figure 1g for a snapshot at $t=1\text{month}$ and Figure 1d of Beucler & Cronin (2018) for a Hovmoller plot of the full time-evolution

² See Figure 4b of Beucler & Cronin (2018) for the time-evolution of the total MSE variance

³ This experiment is very similar to the experiment in which both radiative heating and surface enthalpy fluxes are horizontally uniform (see Figures 1a and 1c of Beucler & Cronin (2018))

Moving to the more realistic NG simulations in Figure 2b, the effect of self-aggregation is qualitatively similar to the LC case if measured by the difference between the full and dotted green lines. That is, removing the spatial variability of radiation (green dotted line) prevents the transient MSE field from developing variance at long wavelengths relative to the control (green solid line). In contrast, removing the spatial variability of surface enthalpy fluxes adds variance at long wavelengths (dashed lines) in both the LC and NG setups, because surface enthalpy fluxes damp developing MSE anomalies after the initial stages of aggregation, opposite to radiation (see Beucler & Cronin, 2018, for an extensive discussion on this topic).

We now turn to our main goal of comparing idealized simulations against observational data. The black line in Figure 2 depicts the observational ERA spectrum, averaged from 10°S to 10°N and over 5 full years (January 1st 2010 – December 31st 2014). The zonal MSE variance is slightly larger in ERA than in the NG CTRL case, except over the range of wavelengths where the NG spectrum peaks ($\lambda \sim 500\text{km} - 2,500\text{km}$). To assess the robustness of our observed spectrum, we recalculate the zonal MSE spectrum over the same latitude range and time period using satellite data (CERES, light blue line). The CERES and ERA spectra agree very well at all wavelengths, although this agreement breaks down at short wavelengths ($\lambda < 1,000\text{km}$) if we do not average the data over one-day blocks (not shown). Hourly ERA data exhibit more spatial variability at short wavelengths, suggesting that CERES data and one-day time-averaging in the NG case may smooth out the MSE variability at short wavelengths. Finally, although the observational MSE spectrum flattens progressively at long wavelengths with no clear maximum, spectra from idealized CPM exhibit a local maximum in the MSE variance at wavelengths of $\sim 1,000 - 5,000\text{km}$. This peak is consistent with the strong $\sim 5,000\text{km}$ Madden-Julian Oscillation-like signal in NG CTRL and NG UNI-SEF (Khairoutdinov & Emanuel, 2018), and the $\sim 2,000\text{km}$ -long moist and dry regions of LC CTRL (Wing et al., 2016; Beucler & Cronin, 2018). In observations, self-aggregation may not appear as a distinct peak in the MSE power spectrum, but simply as an enhancement of MSE variance over a broad range of scales. A peak might not form in the real Tropics for several reasons, including the larger amount of external forcing, lateral mixing, and amplifying diabatic feedbacks operating across a broader range of wavelengths. This motivates a quantitative framework to compare MSE tendencies across scales in models and observations: if the same processes enhance variance at large-scales, then self-aggregation processes likely play an important role in regulating observed MSE spectra.

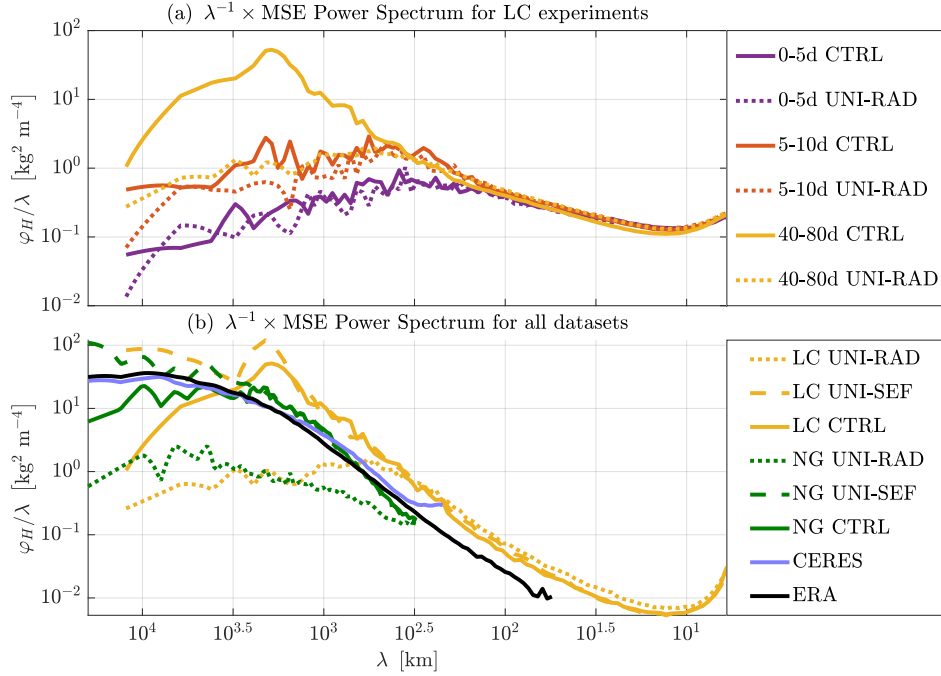


Figure 2. (a) Zonal power spectrum of transient MSE in the LC CTRL experiment (full lines) and the LC UNI-RAD experiment (dotted lines), time-averaged over different stages of the simulation. (b) Zonal power spectrum of transient MSE of all datasets, time-averaged over 40d-80d for the LC experiments and over the entire time period for all other experiments. In both panels, spectra have been averaged over the y -dimension, and divided by λ so that they integrate to the total variance in logarithmic λ -space. To facilitate interpretation, spectra are divided by L_v^2 to yield units $\text{kg}^2 \text{m}^{-4}$. Note that the observed spectra (light-blue and black lines) resemble the aggregated idealized spectra (yellow and green solid lines), but differ from the non-aggregated spectra (yellow and green dotted lines) by more than an order of magnitude at long wavelengths.

3.2 Adapting a Spectral Budget for Model-Observations Intercomparison

We now derive a formal spectral decomposition of the transient MSE budget terms to quantitatively assess the respective roles of separate processes in maintaining the spectrum at each wavelength.

This begins with the transient MSE budget, building on standard approaches, but modified so as to help fairly compare our simulations with observations, thus forging new ground. The transient MSE field H' evolves in response to the net MSE flux at the atmospheric column's boundaries, with contributions from the net longwave flux \dot{H}_{lw} , the net shortwave flux \dot{H}_{sw} , the surface enthalpy fluxes \dot{H}_{sf} and the advection of MSE through the column's boundaries \dot{H}_{adv} . Separating the four MSE tendencies \dot{H}_i into their temporal mean $\overline{\dot{H}_i}$ and their transient component \dot{H}'_i in the same spirit as equation 2, we can write the transient MSE budget as:

$$\frac{\partial H'}{\partial t} = \sum_{i=lw,sw,sf,adv} \dot{H}'_i. \quad (5)$$

Following Section 2.2 of Beucler & Cronin (2018), we take the Fourier transform of Equation 5 and multiply it by the complex conjugate \widehat{H}'^* of Equation 4 to derive a budget for the zonal spectrum φ_H of transient MSE:

$$\frac{1}{2} \frac{\partial \varphi_H}{\partial t} = \sum_{i=lw,sw,sf,adv} \Re \left(\widehat{H}'^* \widehat{H}'_i \right), \quad (6)$$

where \Re is the real part of a complex number. At each wavelength λ , MSE variance is created if a MSE tendency \dot{H}_i increases MSE where the transient MSE anomaly H' is positive, corresponding to a positive co-spectrum $\Re \left(\widehat{H}'^* \widehat{H}'_i \right)$. This framework generalizes the MSE variance framework of Bretherton et al. (2005) and Wing & Emanuel (2014), a particular case of Equation 6 that can be derived by integrating equation 6 across wavelengths before dividing it by the wavelength-integral of φ_H (see Appendix B of Beucler & Cronin, 2018). To yield an equation for the rate at which MSE tendencies maintain the MSE spectrum at each wavelength (in units s^{-1}), we average equation 6 in time over a time-period $t_{\overline{H}}$ and divide it by the time-mean MSE spectrum $\overline{\varphi_H}$ at each wavelength:

$$\frac{1}{t_{\overline{H}}} \frac{\Delta \varphi_H}{\overline{\varphi_H}} = \sum_{i=lw,sw,sf,adv} \frac{2 \overline{\Re \left(\widehat{H}'^* \widehat{H}'_i \right)}}{\overline{\varphi_H}}, \quad (7)$$

where $\Delta \varphi_H$ is the MSE spectrum difference between the beginning and the end of the time-average. We refer to the terms on the right-hand side of equation 7 as components of the spectral MSE variance tendency or, for brevity, as "variance rates".

Since Equation 7 does not explicitly depend on the time-mean zonal structure of the MSE tendencies, we can make direct analogies between observations and zonally-symmetric RCE, which is a key theoretical result of this paper. Note that transient MSE tendencies themselves may be nonlinearly modulated by stationary features of low-level winds, MSE, clouds, among others. Therefore, equation 7 is not a closed theory for MSE transient variability; instead it provides a convenient diagnostic tool to compare the amount of variance injected by each MSE tendency \dot{H}_i across different base states. The left-hand side of equation 7 is small ⁴ when the initial and final spectra φ_H are similar, or when the time-average is taken over a long time-period $t_{\overline{H}}$. In both cases, the four components of spectral MSE variance tendency on the right-hand side of equation 7 approximately balance. Therefore, we can quantitatively compare the four rates of variance injection *across scales* in models and observations.

3.3 Zonal Spectral Budget Intercomparison

The spectral rates of variance injection, depicted in Figure 3, have similar signs and amplitude across models (green and yellow lines) and observations (black and light-blue lines). Surprisingly, even the LC variance rates (yellow lines) have similar signs and amplitudes to the variance rates from planetary-domain experiments, and are simply shifted to shorter wavelengths, despite the smaller zonal extent and 64:1 aspect ratio of the LC configuration. Therefore, we see the LC configuration as an idealized, reduced-size model to study the interaction between convection and the large-scale circulation, which makes LC a promising yet relatively inexpensive framework to study the processes maintaining convective aggregation across climates (Wing et al., 2018).

⁴ The left-hand side of equation 7 equals 0.1% of the longwave variance rate when the ERA dataset is time-averaged over the Jan1,2010–Dec31,2014 period, 1.1% of the longwave variance rate when NG CTRL is time-averaged over 1 year, and 5.1% of the longwave variance rate when LC CTRL is time-averaged over 40-80d.

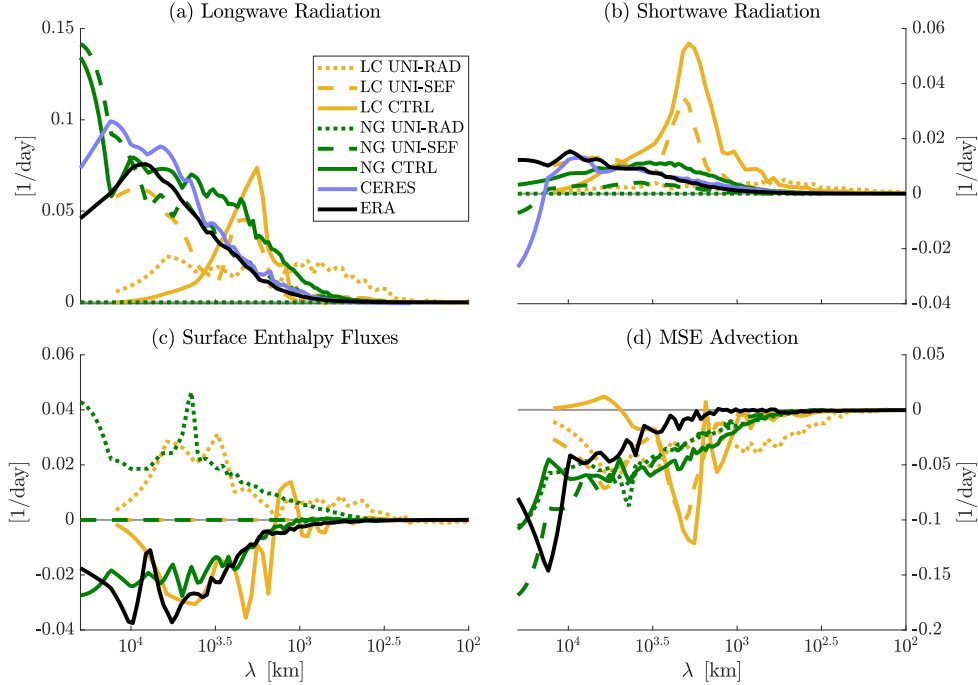


Figure 3. Rate at which (a) longwave radiation (b) shortwave radiation (c) surface enthalpy fluxes and (d) MSE advection maintain the MSE power spectrum at each wavelength (in units day⁻¹) and for all datasets. The UNI-SEF rates of variance injection (dashed lines) have been divided by a factor of 5 because the denominator of equation 7, which is the time-averaged spectrum $\overline{\varphi_H}$, is smaller for non-aggregated simulations. Note the similar signs and shapes of the observed variance rates (light-blue and black lines) and the variance rates from *aggregated* idealized simulations (yellow and green solid lines).

First, since longwave cooling to space is systematically lower in moist regions of high MSE (e.g., Beucler & Cronin, 2016), longwave radiation injects MSE variance at all wavelengths (Figure 3a), with rates as high as 1/ (2 weeks) at the planetary scale. Shortwave heating is larger in moister regions, mostly because of water vapor absorption (e.g., sub-section 3.3 of Wing et al., 2017), resulting in a shortwave injection of MSE variance at all wavelengths (Figure 3b). Surface enthalpy fluxes remove variance in observations and for idealized cases where convection has aggregated, while they unrealistically inject variance for the sensitivity tests (UNI-RAD) in which aggregation is artificially prevented (Figure 3c) or in the early phases of convective self-aggregation (see Appendix D of Beucler & Cronin, 2018). The difference between the rate at which surface fluxes remove variance in the aggregated and non-aggregated cases can be explained by decomposing the surface enthalpy fluxes into a wind-driven component and a component driven by the near-surface enthalpy disequilibrium. Section 3.4 of Beucler & Cronin (2018) shows that while the wind-driven component favors convective aggregation (variance injection) because convective gustiness is higher in convectively-active regions, surface enthalpy disequilibrium is largest in dry regions, damping MSE variance (variance removal). As convection aggregates, MSE variance increases at long wavelengths and so does the surface enthalpy disequilibrium. In the real-world atmosphere, additional factors such as higher near-surface wind speeds (Maloney et al., 2010), ocean heat transport (Benedict & Randall, 2011), and dry air intrusions (Bretherton & Khairoutdinov, 2015) can increase the smoothing effect of the disequilibrium-driven variability of surface enthalpy fluxes, while further decreas-

ing the aggregating effect of the wind-driven variability. This leads to larger surface flux damping at scales where radiation injects the most variance (Figure 3c), and might contribute to the absence of a peak in the ERA MSE spectrum (Figure 2b). MSE advection removes variance at all wavelengths with a maximum removal rate at the planetary scale (Figure 3d). Since total advection is calculated as a residual of equation 7, the fine variability of its variance rate may not be resolved, especially in ERA which does not close the MSE budget; explicitly calculating the horizontal and vertical components of MSE advection from three-dimensional data will be needed to clarify its scale-selectivity in observations and models.

4 Conclusion

The multi-scale patterns of convective aggregation are directly connected to the hydrologic cycle in the Tropics (e.g., Kiranmayi & Maloney, 2011). While convection-permitting models have provided insight into the physical processes controlling convective aggregation, it has been hard to meaningfully compare idealized simulations against observations. We have addressed this issue by applying a spectral technique that reveals scale-selective aggregation processes in meteorological reanalyses, satellite retrievals, and idealized convection-permitting simulations of varying complexity.

The budget for the transient MSE spectrum exhibits scale-selective tendencies that hold across models and observations: longwave radiation injects variance at the longest wavelengths, shortwave radiation injects variance at long wavelengths, MSE advection removes variance across scales, and surface enthalpy fluxes mostly remove variance between $\lambda \approx 1,000\text{km}$ and $\lambda \approx 10,000\text{km}$. We find a stronger damping effect of surface enthalpy fluxes in ERA reanalysis data relative to simulations that neglect ocean interaction and horizontal sea surface gradients. This finding is consistent with recent RCE simulations that have made surface flux feedbacks on aggregation more realistic by adding a meridional surface temperature gradient (e.g., Bretherton & Khairoutdinov, 2015) or increasing surface temperature variability by adding a slab ocean (e.g., Coppin & Bony, 2017; Hohenegger & Stevens, 2016) or soil (e.g., Hohenegger & Stevens, 2018), resulting in a damping of self-aggregation patterns.

Removing the interaction between radiation and water vapor in the simulations prevents convective self-aggregation, resulting in a loss of MSE variance at long wavelengths ($\lambda > 1,000\text{km}$), and corresponding disagreement with the observed MSE variance. This adds to the growing body of evidence that radiatively-driven self-aggregation is key to generating realistic moisture variability from homogeneous boundary conditions (e.g., Arnold & Randall, 2015).

Undoubtedly, aspects of the causality are still murky since vertically-resolved, lower-tropospheric specific humidity, whose variance dominates the column MSE variance (Holloway & Neelin, 2009), may not directly respond to the thermodynamical constraints governing column MSE. For instance, is the longwave variance production peak too high for LC in Figure 3a because cloud-radiation processes are represented incorrectly, or because vertical advection of water vapor amplifies variance too much at a specific length scale? The framework introduced here generalizes to three-dimensional tracer variance budgets, and could be used to investigate the processes injecting zonal variance in the lower-tropospheric water vapor spectrum at long wavelengths.

Ultimately, we hope the tool summarized here can be deployed across the emerging hierarchy of global cloud resolving models (Satoh et al., 2019) to help clarify their intrinsic thermodynamics. Our spectral framework can be generalized to spatially-limited domains by choosing a transform insensitive to non-periodic boundaries, such as the discrete cosine transform (e.g., Denis et al., 2002; Selz et al., 2018). It can also be generalized to arbitrary subsets of the domain by choosing a transform retaining lo-

calization information, such as the wavelet transform (e.g., Torrence & Compo, 1998). While spatio-temporal spectra are familiar to tropical dynamicists (e.g., Wheeler & Kiladis, 1999; Yasunaga et al., 2019), formal spectral decomposition of underlying process budgets are not yet in widespread use. In this context, traditional diagnostic tools may fail to compactly analyze the underlying causes of multi-scale discrepancies across models. By quantifying the preferential scales of zonal thermodynamic variability, our spectral framework allows comparison between models and observational datasets across configurations, resolutions, and scales.

Acknowledgments

Tom Beucler is supported by NSF grants AGS-1520683 and OAC-1835769, Tristan Abbott and Timothy Cronin are supported by NSF grants AGS-1740533 and AGS-1623218, and Mike Pritchard is supported by NSF grant AGS-1734164 and DOE grant de-sc0012152. We thank Kerry Emanuel, Paul O’Gorman, Zhiming Kuang and Chris Bretherton for review and guidance on an early version of this manuscript, and two anonymous reviewers who helped improve the quality of the present manuscript. The source code and data used to produce the figures can be found at https://github.com/tbeucler/2019_Convective_SA_MSE_Transients. The ERA reanalysis data was downloaded from the Copernicus Data Store, the CERES data was downloaded from the CERES NASA website, the NG data is stored on the Cheyenne computing cluster provided by NCAR, and the LC data is stored on the Engaging computing cluster provided by MIT.

References

- Arnold, N. P., & Randall, D. A. (2015, dec). Global-scale convective aggregation: Implications for the Madden-Julian Oscillation. *Journal of Advances in Modeling Earth Systems*, 7(4), 1499–1518. Retrieved from <http://doi.wiley.com/10.1002/2015MS000498> doi: 10.1002/2015MS000498
- Benedict, J. J., & Randall, D. A. (2011, sep). Impacts of Idealized Air-Sea Coupling on Madden-Julian Oscillation Structure in the Superparameterized CAM. *Journal of the Atmospheric Sciences*, 68(9), 1990–2008. Retrieved from <http://journals.ametsoc.org/doi/abs/10.1175/JAS-D-11-04.1> doi: 10.1175/jas-d-11-04.1
- Beucher, F., Lafore, J. P., Karbou, F., & Roca, R. (2014, jul). High-resolution prediction of a major convective period over West Africa. *Quarterly Journal of the Royal Meteorological Society*, 140(682), 1409–1425. Retrieved from <http://doi.wiley.com/10.1002/qj.2225> doi: 10.1002/qj.2225
- Beucler, T., & Cronin, T. (2018, feb). A Budget for the Size of Convective Self-aggregation. *Quarterly Journal of the Royal Meteorological Society*. Retrieved from <http://doi.wiley.com/10.1002/qj.3468> doi: 10.1002/qj.3468
- Beucler, T., & Cronin, T. W. (2016, dec). *Moisture-radiative cooling instability* (Vol. 8) (No. 4). Retrieved from <http://doi.wiley.com/10.1002/2016MS000763> doi: 10.1002/2016MS000763
- Bretherton, C. S., Blossey, P. N., & Khairoutdinov, M. (2005). An Energy-Balance Analysis of Deep Convective Self-Aggregation above Uniform SST. *Journal of the Atmospheric Sciences*, 62(12), 4273–4292. doi: 10.1175/JAS3614.1
- Bretherton, C. S., & Khairoutdinov, M. F. (2015, dec). Convective self-aggregation feedbacks in near-global cloud-resolving simulations of an aquaplanet. *Journal of Advances in Modeling Earth Systems*, 7(4), 1765–1787. Retrieved from <http://doi.wiley.com/10.1002/2015MS000499> doi: 10.1002/2015MS000499
- Coppin, D., & Bony, S. (2017, may). Internal variability in a coupled General Circulation Model in Radiative-Convective Equilibrium. *Geophysical Research Letters*. Retrieved from <http://doi.wiley.com/10.1002/2017GL073658> doi: 10.1002/2017GL073658

- Denis, B., Côté, J., & Laprise, R. (2002, jul). Spectral Decomposition of Two-Dimensional Atmospheric Fields on Limited-Area Domains Using the Discrete Cosine Transform (DCT). *Monthly Weather Review*, *130*(7), 1812–1829. Retrieved from [http://journals.ametsoc.org/doi/abs/10.1175/1520-0493\(2002\)130<1812:sdotda>2.0.co;2](http://journals.ametsoc.org/doi/abs/10.1175/1520-0493(2002)130<1812:sdotda>2.0.co;2) doi: 10.1175/1520-0493(2002)130<1812:sdotda>2.0.co;2
- Feldl, N., Frierson, D. M. W., & Roe, G. H. (2014, mar). The influence of regional feedbacks on circulation sensitivity. *Geophysical Research Letters*, *41*(6), 2212–2220. Retrieved from <http://doi.wiley.com/10.1002/2014GL059336> doi: 10.1002/2014GL059336
- Frigo, M., & Johnson, S. G. (2005). The design and implementation of FFTW3. In *Proceedings of the IEEE* (Vol. 93, pp. 216–231). Retrieved from <http://www.fftw.org/fftw-paper-ieee.pdf> doi: 10.1109/JPROC.2004.840301
- Held, I. M., Hemler, R. S., & Ramaswamy, V. (1993). *Radiative-Convective Equilibrium with Explicit Two-Dimensional Moist Convection* (Vol. 50) (No. 23). doi: 10.1175/1520-0469(1993)050<3909:RCEWET>2.0.CO;2
- Hersbach, H., & H. (2016). The ERA5 Atmospheric Reanalysis. *American Geophysical Union, Fall General Assembly 2016, abstract id. NG33D-01*. Retrieved from <http://adsabs.harvard.edu/abs/2016AGUFMNG33D..01H>
- Hill, K. A., & Lackmann, G. M. (2009, oct). Influence of Environmental Humidity on Tropical Cyclone Size. *Monthly Weather Review*, *137*(10), 3294–3315. Retrieved from <http://journals.ametsoc.org/doi/abs/10.1175/2009MWR2679.1> doi: 10.1175/2009MWR2679.1
- Hohenegger, C., & Stevens, B. (2016, sep). Coupled radiative convective equilibrium simulations with explicit and parameterized convection. *Journal of Advances in Modeling Earth Systems*, *8*(3), 1468–1482. Retrieved from <http://doi.wiley.com/10.1002/2016MS000666> doi: 10.1002/2016MS000666
- Hohenegger, C., & Stevens, B. (2018, may). The role of the permanent wilting point in controlling the spatial distribution of precipitation. *Proceedings of the National Academy of Sciences*, *115*(22), 5692–5697. Retrieved from <http://www.ncbi.nlm.nih.gov/pubmed/29760083><http://www.pubmedcentral.nih.gov/articlerender.fcgi?artid=PMC5984498><http://www.pnas.org/lookup/doi/10.1073/pnas.1718842115> doi: 10.1073/pnas.1718842115
- Holloway, C. E. (2017, jun). Convective aggregation in realistic convective-scale simulations. *Journal of Advances in Modeling Earth Systems*, *9*(2), 1450–1472. Retrieved from <http://doi.wiley.com/10.1002/2017MS000980> doi: 10.1002/2017MS000980
- Holloway, C. E., & Neelin, J. D. (2009, jun). Moisture Vertical Structure, Column Water Vapor, and Tropical Deep Convection. *Journal of the Atmospheric Sciences*, *66*(6), 1665–1683. Retrieved from <http://journals.ametsoc.org/doi/abs/10.1175/2008JAS2806.1><http://dx.doi.org/10.1175/2008JAS2806.1> doi: 10.1175/2008JAS2806.1
- Holloway, C. E., Wing, A., Bony, S., Muller, C., Masunaga, H., L'Ecuyer, T. S., . . . Zuidema, P. (2017, nov). *Observing Convective Aggregation* (Vol. 38) (No. 6). Springer Netherlands. Retrieved from <http://link.springer.com/10.1007/s10712-017-9419-1> doi: 10.1007/s10712-017-9419-1
- Houze, R. A. (2004). *Mesoscale convective systems* (Vol. 42) (No. 4). Retrieved from <http://doi.wiley.com/10.1029/2004RG000150> doi: 10.1029/2004RG000150
- Khairoutdinov, M. F., & Emanuel, K. (2018, oct). Intraseasonal Variability in a Cloud-Permitting Near-Global Equatorial Aqua-Planet Model. *Journal of the Atmospheric Sciences*, *JAS-D-18-0152.1*. Retrieved from <http://journals.ametsoc.org/doi/10.1175/JAS-D-18-0152.1> doi: 10.1175/JAS-D-18-0152.1
- Khairoutdinov, M. F., & Randall, D. a. (2003). Cloud Resolving Modeling of the ARM Summer 1997 IOP: Model Formulation, Results, Uncertainties,

- and Sensitivities. *Journal of the Atmospheric Sciences*, 60, 607–625. doi: 10.1175/1520-0469(2003)060<0607:CRMOTA>2.0.CO;2
- Kiranmayi, L., & Maloney, E. D. (2011, nov). Intraseasonal moist static energy budget in reanalysis data. *Journal of Geophysical Research Atmospheres*, 116(21). Retrieved from <http://doi.wiley.com/10.1029/2011JD016031> doi: 10.1029/2011JD016031
- Laing, A. G., Trier, S. B., & Davis, C. A. (2012, sep). Numerical Simulation of Episodes of Organized Convection in Tropical Northern Africa. *Monthly Weather Review*, 140(9), 2874–2886. Retrieved from <http://journals.ametsoc.org/doi/abs/10.1175/MWR-D-11-00330.1> doi: 10.1175/mwr-d-11-00330.1
- LeMone, M. A., Zipser, E. J., & Trier, S. B. (1998, dec). The Role of Environmental Shear and Thermodynamic Conditions in Determining the Structure and Evolution of Mesoscale Convective Systems during TOGA COARE. *Journal of the Atmospheric Sciences*, 55(23), 3493–3518. Retrieved from [http://journals.ametsoc.org/doi/abs/10.1175/1520-0469\(1998\)055<3493:TROESA>2.0.CO;2](http://journals.ametsoc.org/doi/abs/10.1175/1520-0469(1998)055<3493:TROESA>2.0.CO;2) doi: 10.1175/1520-0469(1998)055<3493:TROESA>2.0.CO;2
- Maloney, E. D., Sobel, A. H., & Hannah, W. M. (2010, apr). Intraseasonal variability in an aquaplanet general circulation model. *Journal of Advances in Modeling Earth Systems*, 2(2), 5. Retrieved from <http://doi.wiley.com/10.3894/JAMES.2010.2.5> doi: 10.3894/JAMES.2010.2.5
- Montgomery, M. T., & Smith, R. K. (2017, jan). Recent Developments in the Fluid Dynamics of Tropical Cyclones. *Annual Review of Fluid Mechanics*, 49(1), 541–574. Retrieved from <http://www.annualreviews.org/doi/10.1146/annurev-fluid-010816-060022> doi: 10.1146/annurev-fluid-010816-060022
- Muller, C., & Bony, S. (2015, jul). What favors convective aggregation and why? *Geophysical Research Letters*, 42(13), 5626–5634. Retrieved from <http://doi.wiley.com/10.1002/2015GL064260> doi: 10.1002/2015GL064260
- Satoh, M., Stevens, B., Judt, F., Khairoutdinov, M., Lin, S.-J., Putman, W. M., & Düben, P. (2019, may). Global Cloud-Resolving Models. *Current Climate Change Reports*, 1–13. Retrieved from <http://link.springer.com/10.1007/s40641-019-00131-0> doi: 10.1007/s40641-019-00131-0
- Selz, T., Bierdel, L., & Craig, G. C. (2018, feb). Estimation of the Variability of Mesoscale Energy Spectra with Three Years of COSMO-DE Analyses. *Journal of the Atmospheric Sciences*, 76(2), 627–637. Retrieved from <http://journals.ametsoc.org/doi/10.1175/JAS-D-18-0155.1> doi: 10.1175/jas-d-18-0155.1
- Stein, T. H., Holloway, C. E., Tobin, I., & Bony, S. (2017, mar). Observed relationships between cloud vertical structure and convective aggregation over tropical ocean. *Journal of Climate*, 30(6), 2187–2207. Retrieved from <http://journals.ametsoc.org/doi/10.1175/JCLI-D-16-0125.1> doi: 10.1175/JCLI-D-16-0125.1
- Tobin, I., Bony, S., & Roca, R. (2012, oct). Observational Evidence for Relationships between the Degree of Aggregation of Deep Convection, Water Vapor, Surface Fluxes, and Radiation. *Journal of Climate*, 25(20), 6885–6904. Retrieved from <http://journals.ametsoc.org/doi/abs/10.1175/JCLI-D-11-00258.1> doi: 10.1175/JCLI-D-11-00258.1
- Torrence, C., & Compo, G. P. (1998, jan). A Practical Guide to Wavelet Analysis. *Bulletin of the American Meteorological Society*, 79(1), 61–78. Retrieved from [http://journals.ametsoc.org/doi/abs/10.1175/1520-0477\(1998\)079<0061:APGTWA>2.0.CO;2](http://journals.ametsoc.org/doi/abs/10.1175/1520-0477(1998)079<0061:APGTWA>2.0.CO;2) doi: 10.1175/1520-0477(1998)079<0061:APGTWA>2.0.CO;2
- Trenberth, K. E., Stepaniak, D. P., & Caron, J. M. (2002, apr). Interannual variations in the atmospheric heat budget. *Journal of Geophysical Research*, 107(D8),

4066. Retrieved from <http://doi.wiley.com/10.1029/2000JD000297> doi: 10.1029/2000JD000297
- Webster, P. J., Magaña, V. O., Palmer, T. N., Shukla, J., Tomas, R. A., Yanai, M., & Yasunari, T. (1998, jun). Monsoons: Processes, predictability, and the prospects for prediction. *Journal of Geophysical Research: Oceans*, *103*(C7), 14451–14510. Retrieved from <http://doi.wiley.com/10.1029/97JC02719> doi: 10.1029/97JC02719
- Wheeler, M., & Kiladis, G. N. (1999). Convectively Coupled Equatorial Waves: Analysis of Clouds and Temperature in the Wavenumber-Frequency Domain. *Journal of the Atmospheric Sciences*, *56*, 374–399. doi: 10.1175/1520-0469(1999)056<0374:CCEWAO>2.0.CO;2
- Wielicki, B. A., Barkstrom, B. R., Harrison, E. F., Lee, R. B., Louis Smith, G., & Cooper, J. E. (1996, may). Clouds and the Earth's Radiant Energy System (CERES): An Earth Observing System Experiment. *Bulletin of the American Meteorological Society*, *77*(5), 853–868. Retrieved from [http://journals.ametsoc.org/doi/abs/10.1175/1520-0477\(1996\)077<0853:CATERE%3E2.0.CO%3B2](http://journals.ametsoc.org/doi/abs/10.1175/1520-0477(1996)077<0853:CATERE%3E2.0.CO%3B2) doi: 10.1175/1520-0477(1996)077<0853:CATERE>2.0.CO;2
- Wing, A., Camargo, S. J., & Sobel, A. H. (2016, jul). Role of radiative-convective feedbacks in spontaneous tropical cyclogenesis in idealized numerical simulations. *Journal of the Atmospheric Sciences*, *73*(7), JAS-D-15-0380.1. Retrieved from <http://journals.ametsoc.org/doi/10.1175/JAS-D-15-0380.1> doi: 10.1175/JAS-D-15-0380.1
- Wing, A., & Cronin, T. W. (2016, jan). Self-aggregation of convection in long channel geometry. *Quarterly Journal of the Royal Meteorological Society*, *142*(694), 1–15. Retrieved from <http://doi.wiley.com/10.1002/qj.2628> doi: 10.1002/qj.2628
- Wing, A., Emanuel, K., Holloway, C. E., & Muller, C. (2017, feb). Convective Self-Aggregation in Numerical Simulations: A Review. *Surveys in Geophysics*. Retrieved from <http://link.springer.com/10.1007/s10712-017-9408-4> doi: 10.1007/s10712-017-9408-4
- Wing, A., & Emanuel, K. a. (2014). Physical mechanisms controlling self-aggregation of convection in idealized numerical modeling simulations. *Journal of Advances in Modeling Earth Systems*, *5*(November), 59–74. Retrieved from <http://dx.doi.org/10.1002/2013MS000269> doi: 10.1002/2013MS000269
- Wing, A., Reed, K. A., Satoh, M., Stevens, B., Bony, S., & Ohno, T. (2018). Radiative-convective equilibrium model intercomparison project. *Geoscientific Model Development*, *11*(2), 793–813. Retrieved from <https://doi.org/10.5194/gmd-11-793-2018> doi: 10.5194/gmd-11-793-2018
- Woodhams, B. J., Birch, C. E., Marsham, J. H., Bain, C. L., Roberts, N. M., & Boyd, D. F. A. (2018, sep). What Is the Added Value of a Convection-Permitting Model for Forecasting Extreme Rainfall over Tropical East Africa? *Monthly Weather Review*, *146*(9), 2757–2780. Retrieved from <http://journals.ametsoc.org/doi/10.1175/MWR-D-17-0396.1> doi: 10.1175/mwr-d-17-0396.1
- Yasunaga, K., Yokoi, S., Inoue, K., & Mapes, B. E. (2019, jan). Space-time spectral analysis of the moist static energy budget equation. *Journal of Climate*, *32*(2), 501–529. Retrieved from <http://journals.ametsoc.org/doi/10.1175/JCLI-D-18-0334.1> doi: 10.1175/JCLI-D-18-0334.1
- Zhang, C. (2005). Madden-Julian Oscillation. *Reviews of Geophysics*, *43*(2004), 1–36. doi: 10.1029/2004RG000158.1.INTRODUCTION